

Preparation, characterization and application of Fe-pillared bentonite to the removal of Coomassie blue dye from aqueous solutions

A. Kadeche^{1,2} · A. Ramdani^{1,3} · M. Adjdir^{4,5} · A. Guendouzi¹ · S. Taleb³ · M. Kaid^{1,2} · A. Deratani⁶

Abstract

This study aims to prepare the sodium bentonite (Bent-Na) and the iron-pillared bentonite (PILC-Fe) and to evaluate its adsorption efficacy against Coomassie blue from aqueous solution. Results demonstrated that the PILC-Fe sample presents an increase in the basal distance d_{001} from 13.66 to 16.93 Å. The presence of the Fe–O and FeOOH functional group band on PILC-Fe was confirmed by FTIR analysis. A clear increase has been observed of the specific surface area from 45.86 to 125.30 m²/g for Bent-Raw and PILC-Fe, respectively, and this increase is greater than 63%. Adsorption of CBB dye into Bent-Na and PILC-Fe was fast, and their adsorption equilibria were reached within 15 and 5 min, respectively. The maximum adsorption capacity for CBB dye is 9.125 mg/g for PILC-Fe, whereas Bent-Na presents a lower adsorption capacity of around 6.848 mg/g. The maximum CBB dye adsorption rate was attained at pH 4.68 for both bentonites. It is observed a difference in the removal efficiency implying that the adsorption of CBB molecule dye was affected by the structure and functional groups of dyes. It is noticed that the adsorption process for CBB dye into Bent-Na and PILC-Fe was better fitted with the linear

✉ A. Ramdani
ramdaniamina010@gmail.com

¹ Department of Chemistry, Faculty of Sciences, University of Saïda, BP 138, 20000 Saïda, Algeria

² Laboratory of Physico-Chemical Studies, University of Saïda, BP 138, 20000 Saïda, Algeria

³ Laboratory of Materials and Catalysis, Faculty of Exact Sciences, Djillali Liabès University, BP 89, 22000 Sidi Bel Abbès, Algeria

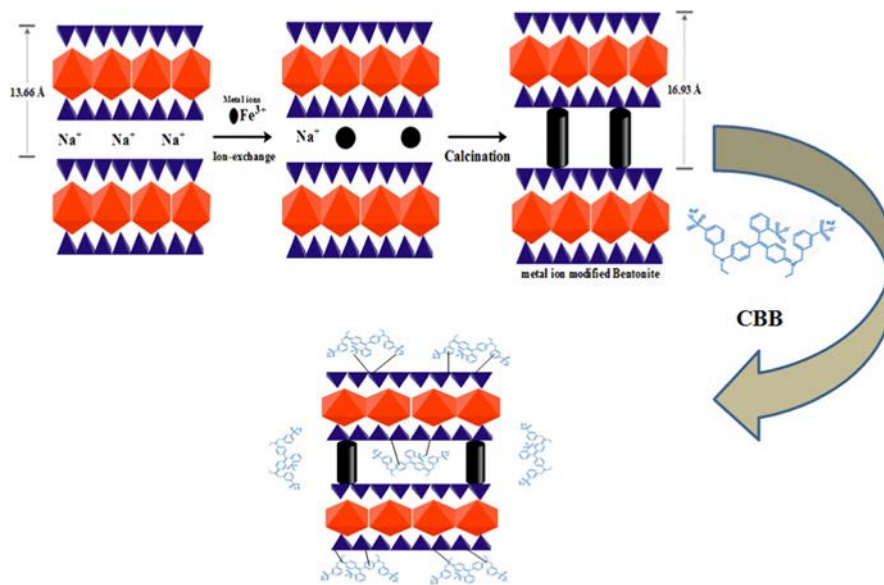
⁴ Department of Engineering Process, Faculty of Technology, University of Saïda, BP 138, 20000 Saïda, Algeria

⁵ Institute of Functional Interfaces Section (IFG), Karlsruher Institute für Technologie (KIT)/Campus Nord, Hermann-von-Helmholtz-Platz 1, 76344 Eggenstein-Leopoldshafen, Karlsruhe, Germany

⁶ Institut Européen des Membranes, ENSCM, Université Montpellier, Montpellier, France

and nonlinear Langmuir model. The CBB dye kinetic adsorption is better fitted by the pseudo-second-order model. Thermodynamic study indicated the feasibility and spontaneity of the CBB dye adsorption process that was exothermic and physical in nature. A comprehensive adsorption and mechanism interaction study of CBB molecular structure onto PILC-Fe was appropriately discussed.

Graphic abstract



Keywords Pillared bentonite · CBB dye · Adsorption study · Wastewater · Mechanism

Introduction

Textile dyes are the most responsible for the ecological and environmental sources of continuous pollution concerns in the world [1, 2]. Therefore, their presence and their use can pose a serious threat to the fauna and flora [3, 4]. There is evidence that many dyes are also known to be carcinogenic and can produce other serious diseases [5]. Dyes are colored organic substances containing many different structural varieties and two main functional groups such as auxochromes group (N₂, NO and NO₂) and chromophoric group (NR₂, NHR, NH₂, COOH and OH) [6, 7]. They are widely used in several industries including food, cosmetic and particularly textile dyeing, because of their chemical stability, ease of synthesis and variety of colors [8, 9]. Nowadays, there are more than ten thousand dyes readily accessible commercially and seven tons of dyes are produced annually [10]. Coagulation and flocculation [11], biodegradation [12], membrane filtration [13], chemical oxidation [14],

ozonation [15], photocatalysis [16–18], ion exchange [19], electrochemical methods [20] and adsorption [9, 21] are famous processes developed and used for the remediation of dyeing wastewater [22]. Adsorption is the most suitable method for the elimination of organic substances, especially dyes; it has become an analytical method of choice, is very effective and is simple in use [23, 24]. Its performance depends on chemical and physical characteristics of adsorbent and adsorbate, its low cost, ease of application, availability, high surface area and non-toxic nature [25]. The principle adsorbent materials were successfully used as an important approach for resolving problem of dyeing wastewater such as: zeolites, activated alumina, apatites, sludge, biomasses, agricultural residues, industrial by-products, activated charcoal and clays [26, 27].

The adsorption of cationic and anionic dyes by different organic and mineral materials has been extensively studied. Naushad et al. [28] synthesized SFGA-modified activated carbon (AGDPA @ AC) and applied it as an adsorbent for the removal of MB dye from aqueous solution. The maximum adsorption capacity was 219.9 mg/g. Anithaa et al. [29] applied the chitosan/PVA composite as an adsorbent for the removal of eosin yellow (EY) dye from the aqueous medium. The results obtained showed that the adsorption capacity was 52.91 mg/g. Wong et al. [30] studied the adsorption of Reactive Black 5 (RB5) and Congo red (CR) from aqueous solution by coffee waste modified with polyethylenimine. The removal rate of RB5 and CR dyes was 99% and 86% with adsorption capacities of 24.8 mg/g and 21.0 mg/g, respectively. The current research is then directed toward low-cost treatment processes using materials such as clays, which may be a good alternative for the adsorption of dyes due to their physicochemical properties, morphology, high surface area, best performance and abundance [31, 32]. In addition, the natural clays possess great adsorption abilities, which results from a net negative charge on their structure, and attract cation organic compounds such as cationic dye removal [24]. Adsorption efficiency can be improved by chemical and physical treatment, purification or modification methods [33, 34]. Nowadays, many researchers [35] are interested in the elaboration of pillared clays. These pillared clays materials are excellent alternative and eco-friendly adsorbents which are strongly used to remove dyes from wastewater and also exhibit potential regenerated adsorbents [36]. PILC are mainly synthesized by cations exchanged into the clay interlayers with single or mixed oligomeric polycations such as Fe, Cr, Al, Co, Cu, Zr, Al–Cu, Al–La, Al–Fe, Al–Si and Zr–Al [33, 34]. The cations exchange leads to the enhancement of basal clay spacing that is substantially larger than the starting clays [35, 37].

In this study, the principal aim is the preparation of Na-bentonite (Na-Bent) and pillared iron bentonite (PILC-Fe) to compare the performance and efficiency of both adsorbents to remove anionic dye Coomassie Brilliant Blue R-250 (CBB) from wastewaters. A comprehensive study on the effect of dye molecular structure by the adsorption onto modified and Fe-pillared bentonite is also investigated by a proposed mechanism.

Experimental

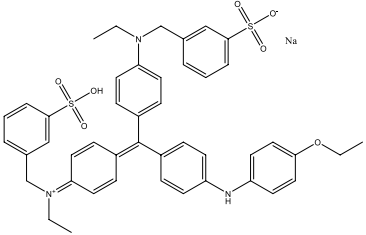
Chemicals

Analytical-grade chemicals are used in these experimental tests, namely: iron (III) nitrate nonahydrate and Coomassie brilliant blue, which were acquired from Sigma-Aldrich (Table 1). All the other chemical reagents, such as sodium chloride, silver nitrate, hydrochloric acid and sodium hydroxide, were obtained from Fluka. In the experiments, individual stock solutions were prepared by dissolving in 1000 mL of deionized water and subsequently diluting to the desired concentration.

Preparation of Bent-Na

The sample clay used in this study was obtained from Maghnia (National Company of Non-Ferrous Mining Products ENOF, northwest Algeria) with a mineralogical composition of about 80 wt% montmorillonite, 10% quartz, 3.0% cristobalite and less than 1% beidellite. Its chemical composition was as follows: 62.48% SiO₂, 17.53% Al₂O₃, 1.23% Fe₂O₃, 3.59% MgO, 0.82% K₂O, 0.87% CaO, 0.22% TiO₂, 0.39% Na₂O, 0.04% As and 13.0% loss on ignition at 950 °C.

Table 1 Physicochemical characteristics of used dyes [38, 39]

Name	Coomassie Brilliant Blue R-250
Chemical structure	
Chemical formula	C ₄₅ H ₄₄ N ₃ NaO ₇ S ₂
Other names	Acid Blue 83; Brilliant indocyanine 6B; Brillantindocyanin 6B; Brilliant Cyanine 6B; Serva Blue R
Family	Triphenylmethanes
Molecular weight (g/mol)	825.97
pKa	1.82
IUPAC name	<i>N</i> -[4-[[4-[(4-Ethoxyphenyl)amino]phenyl][4-[ethyl[(3-sulfophenyl)methyl]amino]phenyl]methylene]-2,5-cyclohexadien-1-ylidene]- <i>N</i> -ethyl-3-sulfobenzenemethanaminium inner salt monosodium salt
CAS number	6104-58-1
λ _{max} (nm)	550

The raw bentonite (Bent-Raw) was treated with 0.5 M HCl and hydrogen peroxide (H_2O_2) to eliminate carbonates and organic matter, respectively. Bent-Raw is filtered, washed and then saturated with sodium chloride solution (1 M) at room temperature for three times. The clay exchanged with sodium was washed and centrifuged to remove chloride ions. The obtained saturated clay is noted (Bent-Na).

Synthesis of PILC-Fe

In order to precipitate the iron hydroxides, the pillaring solutions of Fe were prepared by adding a basic solution of NaOH (1 M) dropwise to the corresponding cationic solution (0.1 M) under constant stirring at room temperature with a discontinuous flow of 1 mL/mn. The Fe/OH molar ratio was 2.5. The solution obtained was aged for 10 days at 25 °C. Therefore, the pillaring solution was added slowly to a dispersion Bent-Na in distilled water 0.5 wt% (w/w) under magnetic stirring at room temperature. The obtained suspension was stirred for 3 h followed by aging at room temperature. Thereafter, the final product was separated by centrifugation and washed with deionized water several times. The exchanged iron Bentonite was calcined at 450 °C to obtain the PILC-Fe.

Characterization methods

The Bent-Raw, Bent-Na and PILC-Fe powders are characterized by X-ray diffraction (XRD) using the Bruker D8 at Cu $K\alpha$ ($\lambda = 1.54060$ nm) radiation at a voltage of 40 kV, and the 2θ range was from 10° to 80°. Fourier transform infrared (FTIR) analysis was performed in a Bruker Alpha spectrometer to record the FTIR spectra of the collected samples (Bent-Raw, Bent-Na and PILC-Fe) and confirm the functional groups over a range of 350–3800 cm^{-1} with a resolution of 1 cm^{-1} . Analysis measurements of the elemental compositions of three materials were obtained using an energy-dispersive X-ray spectrometer (EDS) (Hitachi S-4500). The porous texture of all samples was determined by physical adsorption of N_2 at 77 K, using a Micromeritics ASAP 2000 volumetric adsorption device. The specific surfaces (S_{BET}) of the adsorbent were calculated using the BET (Brunauer–Emmett–Teller) equation assuming that the surface of the nitrogen molecule is 16.2 \AA^2 . The microporous and mesoporous volumes deduced from the data of the N_2 adsorption–desorption isotherms are calculated, respectively, according to the methods of Dubinin–Radushkevich (DR) and Barrett, Joyner and Halenda (BJH), which are given in Table 3. The point of zero charges pH_{PZC} was determined according to a previously reported study [40].

Dye adsorption experiments

Before each adsorption test, the clay samples were dried at 105 °C under vacuum for 24 h. Then, several adsorption experiments were carried out in batch systems by adding an accurate amount of adsorbent (Bent-Na and PILC-Fe) in 100 mL of dye solution to reach equilibrium.

After the equilibrium time was reached, the dispersions were filtered and analyzed. Adsorption equilibrium studies were conducted by varying different controlling parameters such as: the initial dye concentrations from 1 to 100 mg/L; adsorbate mass 50 mg; contact time between solid and liquid 0–120 min; pH varying from 3 to 8; and temperature from 3 to 65 °C. Each adsorption test was done three times, and the average value from results was taken. The percentage dye removal %*R* was calculated as follows:

$$\% \text{ adsorption} = \frac{(C_i - C_{eq})100}{C_i} \quad (1)$$

The adsorption capacity *q* (mg/g) of green malachite was determined by using the following equation:

$$q_e = \frac{X}{m} = \frac{(C_i - C_{eq})V}{m} \quad (2)$$

where *q_e* is the amount of dye adsorbed (mg/g), *C_i* is the initial concentration (mol/L), *C_{eq}* is the equilibrium concentration (mol/L), *V* is the volume of the solution (L), *m* is the mass of adsorbent (g) and *X* is number of grams of dye adsorbed (mg).

In this study, it is necessary to fit the different isotherm models and kinetic equations in order to describe molecular structure of CBB effect on adsorption process. Moreover, the different mathematical models are applied to experimental data in order to find a suitable model which appropriately predicts kinetic and equilibrium isotherm data. The relevant kinetic, equilibrium and thermodynamic equations and parameters used in this study are given in Table 2.

Results and discussion

Characterization

XRD analysis

The powder XRD patterns of (Bent-Raw), (Bent-Na) and pillared clay (PILC-Fe) are given in Fig. 1. The predominant peaks in the Bent-Raw are $2\theta=21^\circ$ and 27° for silica $\text{SiO}_2\alpha$ -quartz $2\theta=6^\circ$, 17.5° , and 20° for the montmorillonite and $2\theta=8^\circ$, 20.70° and 29.36° for the illite. These diffractograms are consistent with those reported by Herbache [40]. Based on the results of diffractogram of Bent-Na, it can be observed there is an increase in basal spacing corresponding to $d_{001}=13.66 \text{ \AA}$ of the sodium bentonite compared to raw bentonite (Bent-Raw) where the $d_{001}=11.39 \text{ \AA}$. This increase can be attributed to the effect of the radius of sodium ions. It is also known that the hydrated radius formed by the sodium ion can reach three spheres of six water molecules compared to other elements such as K^+ , Ca^{2+} , Mg^{2+} and Fe^{2+} [42]. PILC-Fe displays an increase in the basal distance d_{001} from 13.66 for Bent-Na⁺ to 16.93 Å. This increase is due to the intercalation of hydrolyzed iron in the interlayer

Table 2 The kinetic, equilibrium and thermodynamic equations and parameters used in this study [41]

Models	Equation	Parameters
<i>Isotherm models</i>		
Langmuir	$\frac{C_{eq}}{q_e} = \frac{1}{K_L q_m} + \frac{C_{eq}}{q_m}$	q_e (mg/g): equilibrium adsorption capacity q_m (mg/g): maximum adsorption capacity K_L (L/mg): Langmuir constant
Freundlich	$\text{Log } q_e = \text{Log } K_F + \frac{1}{n} C_{eq}$	C_e (mg/L): equilibrium adsorbate concentration in solution n : Heterogeneity factor K_F (mg/g) (L/g): Freundlich constant
Temkin	$q_e = B_T \ln K_T + B_T \ln C_{eq}$	K_T (L/g): Temkin adsorption potential B_T : Temkin constant
Dubinin–Radushkevich (D–R)	$\ln q_e = \ln q_{mDR} - K_{DR} \epsilon^2$ $\left(\epsilon = RT \ln \left(1 + \frac{1}{C_{eq}} \right) \right)$	K_{DR} (mmol ² /J ²): D–R constant ϵ (J/mol): Polanyi potential R : universal gas constant (8.314 J/mol*K) T (K): temperature
<i>Kinetic models</i>		
Pseudo-first-order	$\text{Log}(q_e - q_t) = \text{Log}(q_e) - \left(\frac{K_1}{2.303} \right) t$	q_t (mg/g): amount of adsorbate adsorbed at time t k_1 (1/min): pseudo-first-order rate constant
Pseudo-second-order	$\frac{t}{q_t} = \left(\frac{1}{K_2 q_e^2} \right) + \left(\frac{1}{q_e} \right) t$	k_2 (g/mg ² min): pseudo-second-order rate constant
Elovich	$q_e = \frac{1}{\beta} \ln(\alpha\beta) + \frac{1}{\beta} \ln t$	α (mg/g ² min): initial sorption rate constant β (g/mg): desorption constant
Intraparticle diffusion	$q_t = k_d t^{1/2} + C$	k_1 (mg/g*min ^{1/2}): intraparticle diffusion rate constant C is the film thickness
Thermodynamic parameters	$\ln K_d = \frac{\Delta S_{ads}}{R} - \frac{\Delta H_{ads}}{RT}$ $\Delta G = \Delta H_{ads}^R - T \Delta S_{ads}$	ΔG_{ads} : Gibbs free energy ΔH_{ads} : enthalpy ΔS_{ads} : entropy

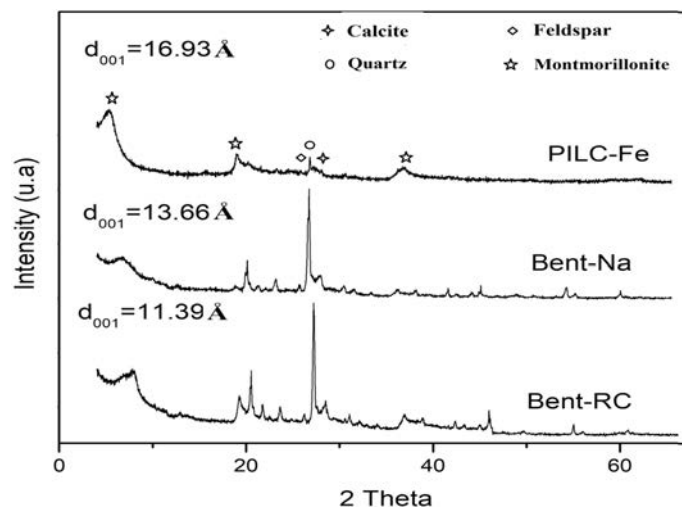


Fig. 1 The XRD patterns of (Bent-Raw), (Bent-Na) and pillared clay (PILC-Fe) samples

spaces of clay via the formation of the pillars. The introduction of different transition metals under different amounts into the basal spacing clay can cause a significant change in XRD patterns, where the position of the 001 reflection can shift toward high or low 2 theta as compared with the reference (raw-bentonite). This effect is linked to the nature of transition metal and their content where a partial disordering of the clay layer arrangement (non-parallel ordering of the clay layers) can occur and causes delaminated structure after calcination [43]. The PILC-Fe retained the typical peaks attributable to montmorillonite phase, whereas the peaks of quartz phase decrease significantly. PILC-Fe exhibited a significantly large basal spacing as compared with other pillared clays. The increase in the basal spacing of Fe-PILC is probably attributed to the large size of polycations (15-30Å) formed by reaction of Na^+ montmorillonite with ferric nitrate under base-hydrolyzed conditions, which was previously reported by Rightor et al. and Pinnavaia et al. [44, 45]. In addition, the typical peak corresponding to 001 reflection of PILC-Fe was very sharp, distinct and well defined, indicating a high crystallinity [45].

Infrared spectroscopy analysis

The infrared spectra of the raw clay Bent-Raw, sodium clay Bent-Na and pillared clay PILC-Fe are shown in Fig. 2; the spectra of (Bent-Raw) indicate the presence of a peak at 3620 cm^{-1} corresponding to the isolated $-\text{OH}$ groups that belong to silanol $\text{Si}-\text{OH}$ and $\text{Al}-\text{OH}$ of the bentonite inner-surface and a wide band centered at 3580 cm^{-1} attributed to germinal and adjacent silanol groups [46, 47]. These bands disappeared in the PILC-Fe which can be attributed to the polymerization of the germinal and the adjacent groups and the formation of the siloxane groups ($\text{Si}-\text{O}-\text{Si}$) due to the calcination step. Another band situated at 1635 cm^{-1} can be assigned to the deformation vibrations of the physically adsorbed water between the

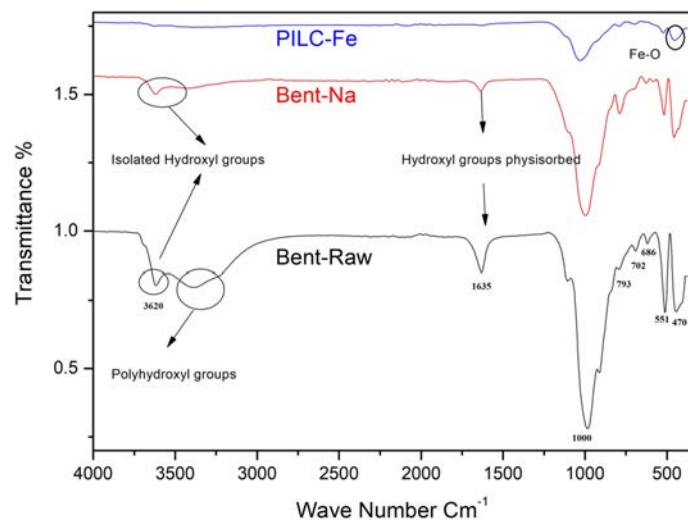


Fig. 2 The infrared spectra of the Bent-Raw, Bent-Na and PILC-Fe samples

spaces [46, 48]. This band seems to be disappeared in PILC-Fe due to the calcination effect. A weakening of the strong band between 900 and 1200 cm^{-1} centered at 1000 cm^{-1} characteristic to the stretching vibrations of Si-O⁻ bonds is very pronounced [49, 50]. This result is supported by N₂ sorption results. It should be also noticed the appearance of new bands at 470 cm^{-1} , 551 cm^{-1} , 686 cm^{-1} and 702 cm^{-1} attributed to Fe-O and FeOOH stretching vibrations [46]. The Fe-O band can also be found in Bent-Raw and Bent-Na characteristic of Fe-rich dioctahedral or trioctahedral smectites. The broad high-intensity band at 1061 cm^{-1} is associated with Si-O-Si antisymmetric stretch, while the band at 964 cm^{-1} is assigned to the Si-O symmetric stretch. The band at 793 cm^{-1} is assigned to the Si-O-Si symmetric stretch [49, 51].

Textural analysis and the zero point charge (ZPC)

Nitrogen adsorption-desorption isotherms of the starting Bent-Raw, Bent-Na and PILC-Fe are presented in Fig. 3. The isotherms of the raw materials were type II according to the IUPAC system [51] related to non-porous materials [52]. Meanwhile, the isotherms of Fe-pillared clay exhibit two different adsorption behaviors, type I at low relative pressures (p/p_0) and type II in high p/p_0 according to the BDDT classification [53] consisting of a mixture of macro- and microporous. The shift of the inflection point "B" in the isotherm of Fe-PLC toward a high relative pressure ($p/p_0=0.4$) indicates an increase in the capacity of adsorption compared to the raw materials. In addition, the hysteresis loop in PILC-Fe was type H₃ according to IUPAC classification [54] typical of slit-shaped pores, indicating that the configuration of parallel plates of clay minerals was fairly preserved [55, 56]. Surface area, porosity and pore size of the Bent-RC, Bent-Na and PILC-Fe samples are given in Table 3. It showed a clear increase in specific surface area. The

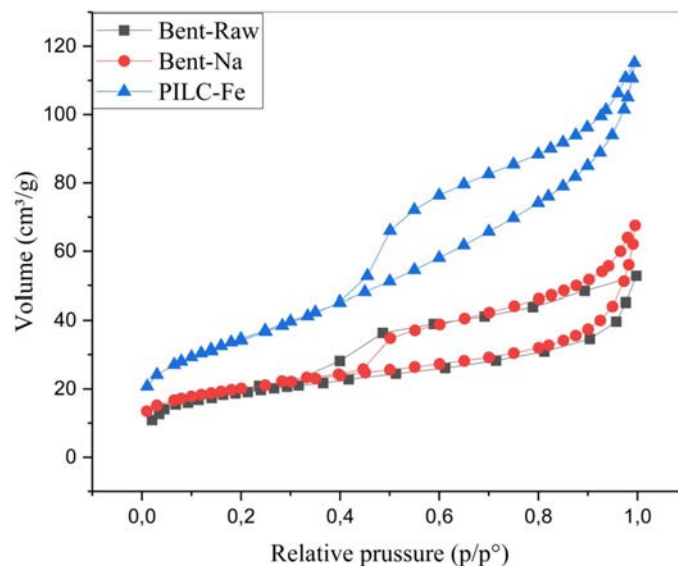


Fig. 3 Nitrogen adsorption–desorption isotherms of the Bent-Raw, Bent-Na and PILC-Fe samples

Table 3 Surface area, porosity and pore size of the Bent-Raw, Bent-Na and PILC-Fe samples

Sample	S_{BET} (m ² /g)	BJH pore volume (cm ³ /g)	4 V/A by BET (Å)	BJH pore diameter (Å)	Total pore volume (cm ³ /g)
Bent-RC	45.86	0.066	42.5214	96.4122	0.05632
Bent-Na	71.18	0.089	44.5113	92.202	0.079207
PILC-Fe	125.30	0.167	50.1291	62.791	0.157026

specific surface area of Bent-Raw is 45.86 m²/g typical to the specific surface area of bentonite; however, this specific surface area increases to 71.18 m²/g when the raw bentonite is exchanged with sodium chloride; this increase can be attributed to a homogenization of basal space of raw bentonite. In the case of PILC-Fe, the specific surface area reached 125.30 m²/g with an increase up to 63% compared to raw bentonite. This increase is a consequence of the effect the creation of iron oxide pillars within the basal spacing which subsequently created two different types of macro- and micropores. This variety of pores has led to an increase in adsorption capacity. This statement is also supported by the pore volume results where the PILC-Fe has the highest value around 0.167 cm³/g.

The zero point charge (ZPC) of PILC-Fe is found to be close to 5.1. Meanwhile, it is expected that anionic dye adsorption will be advantaged under the value pH 5.1 for iron-pillared Bentonite. Furthermore, the sodium Bentonite indicates the zero point charge at pH 5.86. The sodium exchanged process increases mostly isoelectric point charge of the bentonite toward higher pH.

SEM-EDS analysis

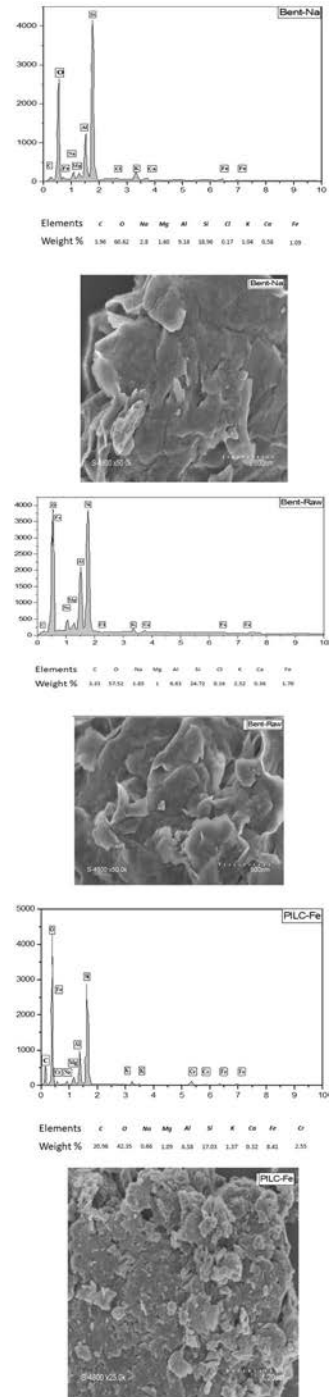
The SEM micrographs of the Bent-Raw, Bent-Na and PILC-Fe are shown in Fig. 4. It can be observed that Bent-Raw and Bent-Na present lamellar structure with a sharp edge. The iron polyoxocations into the bentonite (PILC-Fe) alter the original lamellar structure of Bent-Na and led to the formation of dispersed grain of slit-shaped pores. The individual grain sizes were found to be predominantly in the range of 100–200 nm (Fig. 4) and might contribute to enhancement of specific surface area of PILC-Fe. The quantitative elemental analysis EDX of Bent-Na and Bent-Raw samples is given in Fig. 4. The major elements found in three clay materials are O, Al, Si, Ca, Fe, Cl, Mg and Na. The sodium ion (Na) is a substantial amount in Bent-Na after sodium homoionization. On the basis of the EDX results, it is observed that Fe content in Bent-Na and PILC-Fe was raised from 1.7 to 8.41%, respectively (Fig. 4). This could be explained by the maximum iron exchange with sodium Bentonite, which leads to the well pillars formation during the calcination process.

CBB dye adsorption

Effect of contact time

Dye adsorption onto clay materials is often described as a process depending on the reaction time which may provide information on the kinetic and mechanism adsorption process [57]. Figure 5 indicates the adsorption of CBB dye by sodium and iron-pillared clay as a function of contact time. It is observed that the adsorption of CBB increased with both clay Bent-Na and PILC-Fe in contact time within 15 min and 5, respectively. The obtained results revealed also that the adsorption kinetics is rather fast for PILC-Fe than for Bent-Na. The maximum adsorption capacity for CBB dye is 9.125 mg/g for PILC-Fe, whereas Bent-Na presents a lower adsorption capacity of 6.848 mg/g. Initially, the rate of removal efficiency was rapid due to the adsorption of CBB dye molecules onto the adsorbents. This can be attributed to the presence of a large number of adsorption sites located globally on the Bent-Na, and it leads to reaching the adsorption equilibrium quickly. In the case of the pillared clay, the CBB molecule dyes are absorbed into the interlamellar space and edges. The adsorption rate was very rapid during the initial contact time due to the availability of active adsorption sites at the surface and edges of Bent-Na. Moreover, no significant changes were observed in the percentage of removal of the dyes after equilibrium. Similarly, the percentage removal was constant after equilibrium due to the slow pore diffusion or saturation of adsorbent and the adsorption percentage was stable at a higher time. Table 4 presents a comparison of maximum adsorption capacity (q_e) of the CBB dye on various adsorbents from aqueous solutions. Overall, it can be noticed that bentonite is mainly available and inexpensive adsorbent, with different adsorptive properties, high surface area and high ion exchangeability which may successfully eliminate dyes. Indeed, Anirudhan et al. and Gamoudi et al. [21,

Fig. 4 The SEM–EDX analysis of the Bent-Raw, Bent-Na and PILC-Fe samples



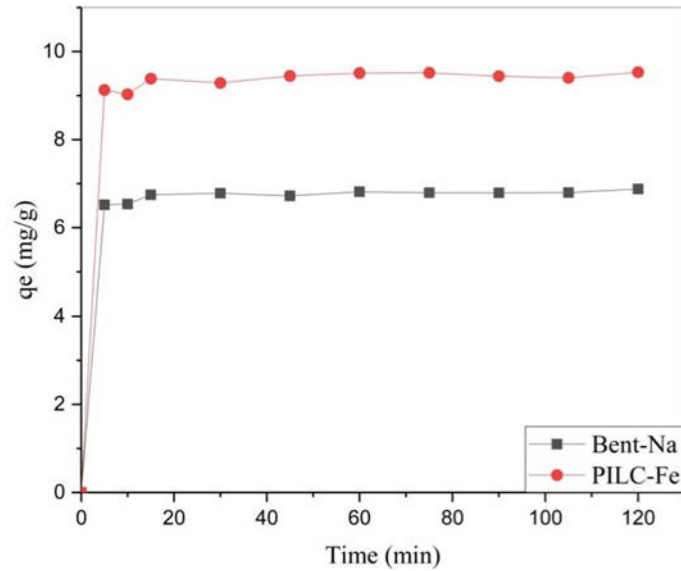


Fig. 5 Effect of contact time on CBB dye adsorption by Bent-Na and PILC-Fe

Table 4 Comparison of maximum adsorption capacity at equilibrium (q_e) of sodium and iron-pillared clay for CBB dye with different adsorbents	Adsorbent	q_e (mg/g)	References
	Apricot stone activated carbon	10.09	[58]
	Wheat bran	6.40	[59]
	α -Chitin nanoparticles	8.55	[60]
	PANI-NiFe ₂ O ₄ magnetic nanocomposite	4.09	[61]
	TiO ₂ /SiO ₂	9.47	[62]
	NiO nanoparticles	11.21	[63]
	Fe ₃ O ₄ @C nanoparticles	11.22	[64]
	Sodium bentonite	6.848	This study
	Iron-pillared bentonite	9.125	This study

57] recorded that pillared clays are convenient materials and seem to be a promising solution for the removal of dyes molecules from industrial wastewater.

Effect of pH

The molecular structure of dyes depends on the pH medium, which consequently leads to a variation in the kinetic and equilibrium adsorption process. CBB dye molecule presents different protonated species with different charges: the zwitterion (CBB \pm) at pH 7 and the positively charged species, CBBH⁺ and CBBH₂²⁺ at pH < 7 [65]. Different types of interactions have been noticed between adsorbents and dyes during adsorption processes such as adsorbent–dye, dye–dye interactions, chemical

bond, hydrogen bonds, van der Waals force, ion exchange and hydrophobic attractions [57]. To study the effect of pH on the adsorption efficiency of sodium and pillared bentonite (Bent-Na and PILC-Fe), experiments were carried out by varying the pH of the solution from 2 to 8.2. Figure 6 shows that the adsorption increases at pH 4.68 and then decreases significantly for more alkaline pH. The effect of pH is more remarkable for PILC-Fe. It was found that the high dye removal efficiency of initial concentrations of 50 mg/L at pH 4.68 was 85.62%, and 97.58% for CBB dye molecules, respectively.

In an acid medium, it is noteworthy that the negative charges of the sulfonate dye groups will be neutralized by H^+ of the acid medium. This phenomenon is not an isolated case but is also observed with chromophore groups [66]. It is known that most of the H^+ ions are consumed by different attractive dye sites. However, the remaining amount of H ions in the solution is absorbed by the defect tetrahedral silanol and aluminol sites (Brönsted and Lewis acid sites) of bentonite. At low pH and below zero potential charges (ZPC), the surface of sodium clay becomes partially negative charged which creates a combined interaction with CBB dye molecules under the global charge of (-1) that promotes its adsorption efficiency. However, at alkaline conditions and above pH (ZPC), the dye is absorbed by the active sites of OH groups of bentonite deprotonated which creates a negative charge. Also, the competition of H ion with the anionic dye species becomes negligible. Furthermore, it can be assumed that the attraction can take place between the OH ions which interact with the positive carbon charges of the dye CBB to form a C–OH bond ($n-\pi$ interaction) [67]. Thus, the interaction between adsorbent and CBB dye decreased, leading to lower removal efficiency. Hence, pH 4.68 seems to be the most suitable for subsequent experiments. The PILC-Fe creates more reactive sites and

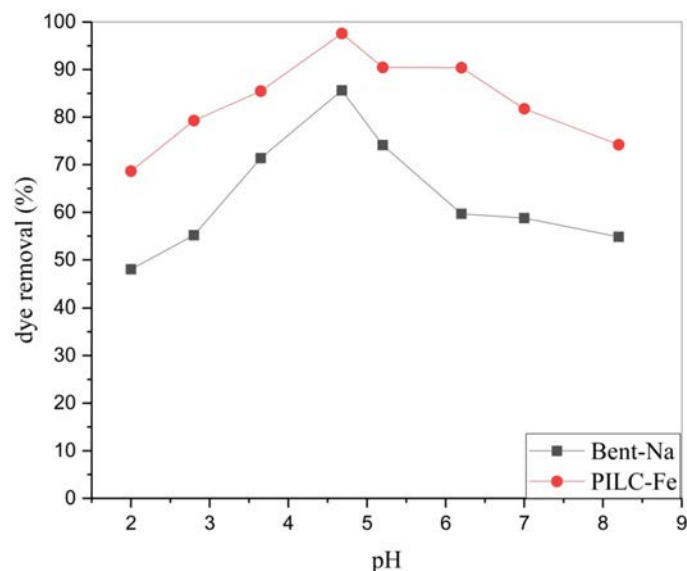


Fig. 6 Effect of pH on CBB dye adsorption by Bent-Na and PILC-Fe

enhances the porosity than sodium bentonite (Bent-Na), which leads to the increase in specific surface area. This result is confirmed by the N_2 sorption analysis. It can be also noticed that CBB dye species were absorbed into the micro- and macropores of iron-pillared clay, followed by an interaction between the sulfonate and chromophore groups of the dye and by the defect bentonite sites (Brönsted and Lewis acids). One cannot neglect the possibility of iron leaching from PILC-Fe under different pHs; however, this phenomenon is still minor and does not affect the PILC-Fe structure. It can be concluded that the PILC-Fe can be considered as a promising candidate for catalyst and decontamination of waste water from different kinds of pollutants [68].

Isothermal adsorption modeling

The adsorption isotherms were utilized adjusted mathematically to four linear and nonlinear models, namely Langmuir, Freundlich, Temkin and Dubinin–Radushkevich (D–R), which were fitted to the experimental equilibrium data for BBC dye. For the nonlinear forms, the four isotherms are plotted using the relation of q_e as a function of C_{eq} as shown in Figs. 7 and 8 after adsorption tests. It is observed that the analysis of the isotherms shows that the adsorption capacity increases with the initial concentration. A remarkable difference was observed in the amount of CBB dye adsorbed by both bentonites. The highest recorded rate of adsorption was observed for PILC-Fe. It can be noted from the graphs representing the adsorbed quantity versus the equilibrium concentration $q_e = f(C_e)$ that the isotherms show a steady state value indicating the saturation of the surface and

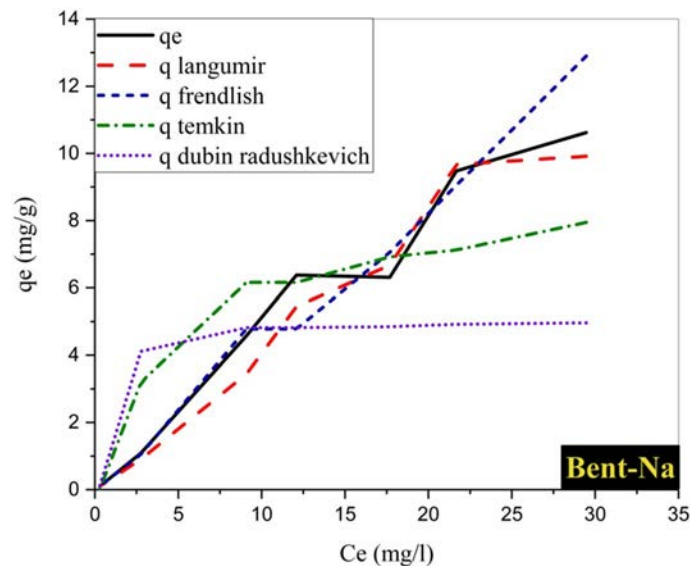


Fig. 7 The four isotherms nonlinear plotted using the relation of q_e as a function of C_{eq} for CBB dye adsorption by Bent-Na

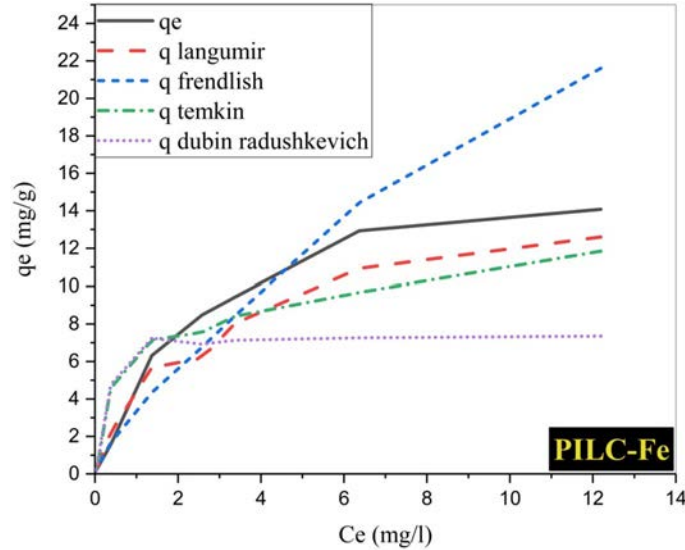


Fig. 8 The four isotherms nonlinear plotted using the relation of q_e as a function of C_{eq} for CBB dye adsorption by PILC-Fe

therefore formation of a monolayer; this is facilitated by the adsorbate–adsorbate interactions in the sub-layer and the adsorbate-adsorbent interactions on the surface. On the other hand, the linearized forms of Langmuir, Freundlich, Temkin and Dubinin–Radushkevich models are applied to check which isotherm is accurate for modeling the adsorption isotherms with different initial concentrations studied (Table 2). The Langmuir isotherm constants K_L and q_m were calculated from the slope and intercept of the plot between $1/q_e$ and $1/C_{eq}$. The Freundlich isotherm assumes that adsorption is multilayer and that the surface of the adsorbent is heterogeneous. The Freundlich isotherm constants K_F and $1/n$ were also determined from the intercept and slope of the plot $\log q_e$ versus $\log C_{eq}$. The empirical constant n indicates the favorability of the adsorption process. K_T and b_T are the equilibrium constants corresponding to the heat and binding energy of adsorption process and were calculated from the intercept and slope of the plot between q_e and $\ln C_{eq}$. D–R isotherm model is another empirical model which mainly elucidates the dye molecule adsorption mechanism with a Gaussian energy distribution onto a heterogeneous surface of adsorbents. ϵ is the Polanyi potential related to equilibrium. The line plots between $\ln q_e$ and ϵ^2 determine K_{D-R} which is the D–R isotherm constant and designated as the mean free energy of adsorption per mole of adsorbate. q_{mD-R} is the theoretical saturation capacity (mg/g).

R_L is another important parameter of the Langmuir isotherm which can be expressed in terms of a dimensionless constant, named the separation factor or equilibrium parameter. It can be defined by the following equation:

$$R_L = \frac{1}{1 + K_L * C_0} \quad (3)$$

A separation factor $R_L > 1$ shows that the adsorption is unfavorable, if $R_L = 1$ the adsorption is in linear form, the adsorption can be favorable when $0 < R_L < 1$, and a zero separation factor ($R_L = 0$) indicates that adsorption is irreversible [57].

E is the mean energy (kJ/mol) which gives information if adsorption process is physical or chemical in nature. If the value of E was higher than 8 kJ/mol, the adsorption is physical in nature, between 8 and 16 kJ/mol, the adsorption process is governed by ion exchange mechanism, while if the values were lower than 16 kJ/mol, the adsorption process is followed by chemical mechanisms [41]. It can be calculated using the following equation:

$$E = \frac{1}{\sqrt{2K_{D-R}}} \quad (4)$$

Based on the obtained correlation coefficients (R^2), the experimental adsorption data fitted better with Langmuir model than Freundlich, Temkin and D–R models in the both cases for Bent-Na and PILC-Fe, suggesting that the adsorption data were well depicted by Langmuir isotherm. This latter assumes that the adsorption phenomena also obeyed monolayer CBB dye molecule adsorption without any mutual interactions at particular homogenous sites on surface of clay adsorbents with identical energies (Figs. 7 and 8). The validity of the isotherm models is in the following order: Langmuir > Temkin > Freundlich > Dubinin–Radushkevich. The values of constant $1/n$ in the Freundlich isotherm were found in the range 0–1, which shows a favorable physical adsorption [38, 57]. Furthermore, the obtained values of separation factor RL from the Langmuir model were in the range between 0.695 and 0.996 and 0.117 and 0.764 for Bent-Na and PILC-Fe, respectively, implying favorable adsorption of CCB dye molecules onto the both sodium and iron-pillared clays. For the D–R isotherm, it is observed that the values of average free energy (E) are found lower, positive and less than 8.0 kJ/mol of 0.794 and 3.436 kJ/mol, suggesting that the mechanism of CCB dye adsorption was physical in nature due to weak electrostatic forces or van der Waals attractions (Table 5). Additionally, the maximum adsorption capacities for CCB dye molecules onto Bent-Na and PILC-Fe given by D–R isotherm (q_{mD-R}) were 4.894 and 7.361 mg/g, respectively, which were lower than those determined from Langmuir isotherm 5.326 and 8.985 mg/g, respectively.

Adsorption kinetics modeling

To better understand the adsorption mechanism of CBB dye molecules onto sodium and iron-pillared clays, the linear form of pseudo-first-order, pseudo-second-order, Elovich and intraparticle diffusion kinetic models was used using equations defined in Table 2. The obtained values of the adsorbed quantities q_e , the kinetic constants K_1 , K_2 , K_d , α , β and the regression coefficients R^2 are given in Table 6.

The R^2 values were found to be relatively low 0.441 and 0.434. The calculation of q_e shows that the calculated adsorbed quantities of CBB dye are very low

Table 5 Isotherm models for CBB dye adsorption by Bent-Na and PILC-Fe

Dye	Langmuir			Freundlich			Temkin			Dubinin-Radushkevich					
	q_m	K_L	R_L	R^2	$1/n$	K_F	R^2	K_T	B_T	R^2	q_{mD-R}	K_{D-R}	R^2	E	$q_{e,exp}$
Bent-Na	5.926	0.013	0.695-0.995	0.999	1	0.383	0.992	0.889	0.388	0.882	4.894	$2.89 \cdot 10^{-7}$	0.913	0.794	6.848
PILC-Fe	8.985	0.87	0.117-0.764	0.998	0.741	3.389	0.972	0.002	0.382	0.896	7.361	$426 \cdot 10^{-8}$	0.871	3.436	9.525

Table 6 Parameters identified by the kinetic models for CBB dye adsorption by Bent-Na and PILC-Fe

Dye	Pseudo-first-order			Pseudo-second-order			Intraparticle diffusion			Elovich			
	K_1	q_e	R^2	K_2	q_e	R^2	$q_{e,exp}$	K_3	C	R^2	α	β	R^2
Bent-Na	0.024	0.627	0.441	0.314	6.896	0.999	6.848	0.032	6.516	0.711	17.362	10.309	0.798
PILC-Fe	0.032	0.970	0.434	0.298	9.524	0.999	9.525	0.044	9.061	0.647	2.718	7.518	0.719

compared to the experimentally adsorbed quantities. These values confirm that the pseudo-first-order model is not a valid one to describe the dye molecule mechanism adsorption by the both bentonite sodium and iron pillared. These observations indicate that the adsorption of CBB does not express a controlled diffusion process since it does not follow the pseudo-first-order equation given by Lagergren. According to Table 6, the pseudo-second-order models fit better the experimental data than that of the pseudo-first-order, the Elovich and the intraparticle diffusion kinetic models, obtaining correlation coefficients higher than 0.999. Additionally, the experimentally adsorbed quantities at equilibrium 6.848 and 9.525 mg/g were found to be in excellent agreement with those calculated from the second-order reaction kinetics equation 6.896 and 9.524 mg/g for Bent-Na and PILC-Fe, respectively. These values confirm the validity of the pseudo-second-order kinetic model to evaluate the adsorptive removal of CBB dye from aqueous solution by the both clays.

Thermodynamic study

The thermodynamic parameters, such as the standard free energy change (ΔG_{ads}), enthalpy change (ΔH_{ads}) and entropy change (ΔS_{ads}) of adsorption, were calculated using the equations defined in Table 2.

The apparent equilibrium constant (K_d) of adsorption is defined as:

$$K_d = \frac{q_e}{C_{\text{eq}}} \quad (5)$$

where q_e and C_{eq} are the adsorbed quantity of CBB dye on the adsorbent and the residual CBB dye concentration at equilibrium, respectively.

The values of ΔH_{ads} and ΔS_{ads} were computed from the slope and intercept of the straight line graph of $\ln K_d$ versus $1/T$. The values of these thermodynamic properties are given in Table 7. From the obtained results, the negative values of ΔH_{ads} (-20.26 to -21.24 kJ/mol) confirm the exothermic character of the adsorption process, whereas the small values found suggest that adsorption is a physical phenomenon. The negative values of free energy ΔG (-38.07 to -48.74 kJ/mol) confirm the spontaneous nature of adsorption [40, 41]. It is also easy to notice that for different adsorbents, ΔG_{ads} decreases with the increase in the solution temperature. This can be explained by the fact that the adsorption process becomes increasingly faster.

The positive value of the standard entropy change ΔS_{ads} (from 0.06 and 0.08 kJ/K.mol shows the increasing randomness at the solid/liquid interface during the absorption of CBB dye molecules in aqueous solution, i.e., it indicates the affinity of the

Table 7 Thermodynamic parameters of CBB dye adsorption process

	ΔH (kJ/mol)	ΔS (J/mol K)	ΔG (kJ/mol)				
			276 K	285 K	295 K	313 K	338 K
Bent-Na	-20.26	0.064	-38.07	-38.65	-39.29	-40.45	-42.07
PILC-Fe	-21.24	0.08	-43.51	-44.27	-45.11	-46.63	-48.74

adsorbent for the removal of CBB dye and the release of hydroxyl groups from the adsorbent surface and into the interlamellar space in the bulk solution. In summary, the adsorption of CBB dye on different adsorbents is a physical and spontaneous process, which is characterized by its reversibility by the speed to reach equilibrium and the release of dye molecules to cover the entire area and not just the specific sites.

Adsorption mechanism

The proposed adsorption mechanism of the CBB dye on the Bent-Na surface and the interlayer space of PILC-Fe can be related to different interaction modes, as shown in Fig. 9. The electrostatic attraction between the negatively charged sulfonate groups (SO_3^-) CBB dye with Fe_2O_3 particles that constitute the pillars (Fig. 9a). In addition, the electrostatic attractions (Fig. 9b) between the positively charged proton functional $\text{Si}(\text{OH})_2$ and $\text{Al}(\text{OH})_2$ sites occurred on both surface Bent-Na and PILC-Fe.

There are two hydrogen bonds [66], namely the hydrogen dipole–dipole H-bond and the Yoshida H-bond. Dipole–dipole H-bond interactions (Fig. 9b) can occur between hydrogen on the surface and the edges of Bent-Na and PILC-Fe with

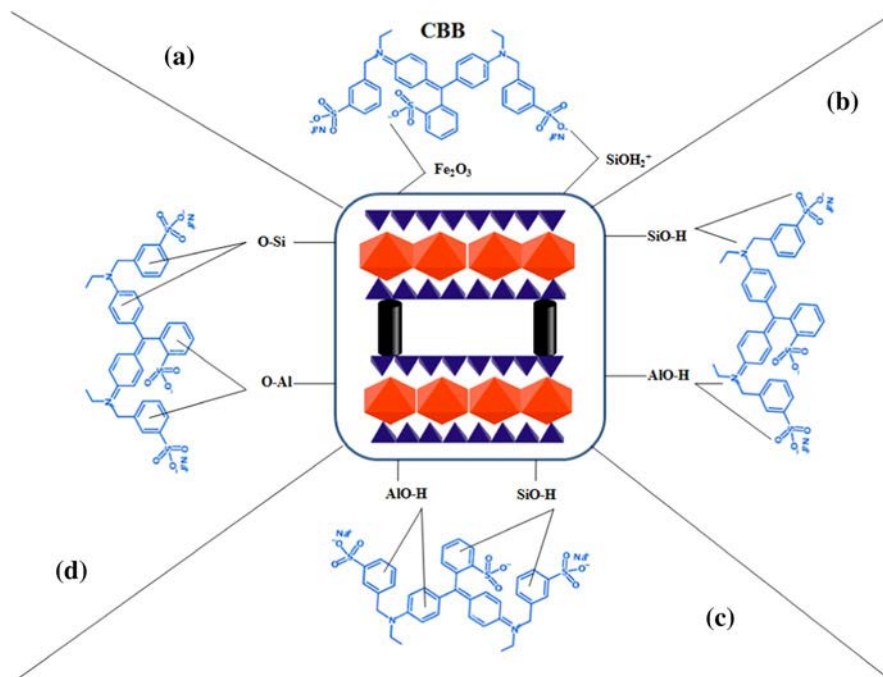


Fig. 9 The possible interaction mechanism proposed between Na-Bent, PILC-Fe and CBB dye: **a** electrostatic attraction, **b** dipole–dipole hydrogen bonding interactions, **c** Yoshida H-bonding and **d** $n-\pi$ stacking interactions

the atoms of O and N of CBB dye, while the Yoshida H bond (Fig. 9c) can occur between OH on the surface of Bent-Na and the structure of PILC-Fe and the ring of aromatic dye.

Finally, the interaction $n-\pi$ (Fig. 9d) occurred by the delocalization of the electron pair isolated from the oxygen atom in the orbital π of the aromatic ring [59, 66].

Conclusion

In this study, the iron-pillared bentonite (PILC-Fe) was synthesized and tested to remove Coomassie blue dye from aqueous solution which was compared with sodium bentonite (Bent-Na). The effect of the molecular structure of Coomassie brilliant blue (CBB) on the Bent-Na and PILC-Fe adsorption was investigated. Results demonstrated that the PILC-Fe sample presents an increase in the basal distance d_{001} from 13.66 Å (Bent-Na) to 16.93 Å, and the appearance of a new pic at 2θ 34° confirms the formation of hematite within the basal spacing of bentonite. The presence of the Fe–O and FeOOH functional group band on PILC-Fe was confirmed by FTIR analysis. A clear increase has been observed of the specific surface area from 45.86 to 125.30 m²/g for Bent-Raw and PILC-Fe, respectively; this increase is greater than 63%. It can be also observed that Fe content in Bent-Na and PILC-Fe is enhanced from 1.7 to 8.41%, respectively, which leads to the formation of the well-defined pillars during the calcination process. The adsorption of CBB dye into Bent-Na and PILC-Fe was fast, and their adsorption equilibrium was reached within 15 and 5 min, respectively. The effect of pH on CBB dye adsorption by both bentonites was significant. The maximum adsorption rate of the CBB dye was reached at pH 4.68, suggesting that the adsorption of the CBB dye by sodium and pillared bentonite could be controlled by an electrostatic interaction mechanism. It is also observed a difference in the removal efficiency, implying that the adsorption of CBB molecule dye was affected by the structure and functional groups of dye. It is noticed also that Langmuir isotherm was found to have the greatest regression data and thus the best-fit model which exhibited a good correlation between experimental data and those calculated by Langmuir's model. The monolayer adsorption capacity of the Bent-Na and PILC-Fe calculated by the Langmuir isotherm was 5.926 and 8.985 mg/g, respectively. Thermodynamic parameters ($H_{\text{ads}} < 0$ and $G_{\text{ads}} < 0$) revealed the feasibility and spontaneity of the CCB dye adsorption process that was exothermic and physical in nature. The adsorption interaction mechanism of CCB molecular structure by Bent-Na and PILC-Fe was investigated and can be determined by various interactions, such as electrostatic attraction, $n-\pi$ stacking and H-bonding. The pillared bentonite proved to be interesting materials to remove dyes from aqueous solution, making the adsorption process effective and less expensive.

Acknowledgements Financial support for this work from The General Directorate of Scientific Research and Technological Development (DGRSDT) and the Ministry for Higher Education and Scientific Research is gratefully appreciated. The authors also thank the European Institute of Membranes University Montpellier France for the realization of this work.

References

1. C. Li, H. Xia, L. Zhang, J. Peng, S. Cheng, J. Shu, S. Zhang, *Res. Chem. Intermed.* **44**, 2231 (2018)
2. Y.N. Kavil, Y.A. Shaban, S.S. Alelyani, R. Al-Farawati, M.I. Orif, M.A. Ghandourah, M. Schmidt, A.J. Turki, M. Zobidi, *Res. Chem. Intermed.* **46**, 755 (2020)
3. P. Velmurugan, J. Shim, B.-T. Oh, *Res. Chem. Intermed.* **42**, 5937 (2016)
4. M. Hasanpour, M. Hatami, *J. Mol. Liq.* **309**, 113094 (2020)
5. Y. Liu, Y. Zhao, W. Cheng, T. Zhang, *J. Colloid Interface Sci.* **579**, 766 (2020)
6. M. Madhura, V. Gayathri, *J. Photochem. Photobiol. A Chem.* **376**, 269 (2019)
7. S. Thota, S.R. Tirukkavalluri, S. Bojja, *J. Catal.* **2014**, 1 (2014)
8. M. Salleh, D. Khalid Mahmoud, W. Abdul Karim, W. Idris, *Desalination* **280**, 1 (2011)
9. I. Feddal, A. Ramdani, S. Taleb, E.M. Gaigneaux, N. Batis, N. Ghaffour, *Desalin. Water. Treat.* **52**, 2654 (2014)
10. B. Padhi, *Int. J. Environ. Sci.* **3**, 940 (2012)
11. S.S. Moghaddam, M.A. Moghaddam, M. Arami, *J. Hazard. Mater.* **175**, 651 (2010)
12. R. Saratale, G. Saratale, D. Kalyani, J.-S. Chang, S.P. Govindwar, *Bioresour. Technol.* **100**, 2493 (2009)
13. J. Yun, Y. Wang, Z. Liu, Y. Li, H. Yang, Z.L. Xu, *Chemosphere* **259**, 127390 (2020)
14. H.D. Bouras, Z. Isik, E.B. Arikian, N. Bouras, A. Chergui, H.C. Yatmaz, N. Dizge, *Biochem. Eng. J.* **146**, 150 (2019)
15. A. Khataee, A. Fazli, F. Zakeri, S.W. Joo, *J. Ind. Eng. Chem.* **89**, 301 (2020)
16. R. Cherrak, M. Hadjel, N. Benderdouche, M. Adjdir, A. Mokhtar, K. Khaldi, A. Sghier, P.G. Weidler, *Silicon* **12**, 927 (2020)
17. G. Sharma, A. Kumar, M. Naushad, A. Kumar, A. Al-Muhtaseb, P. Dhiman, A.A. Ghfar, F.J. Stadler, M.R. Khan, *J. Clean. Prod.* **172**, 2919 (2018)
18. M. Naushad, G. Sharma, Z.A. Allothman, *J. Clean. Prod.* **241**, 118263 (2019)
19. Z. Zhu, M. Zhang, F. Liu, C. Shuang, C. Zhu, Y. Zhang, A. Li, *J. Taiwan. Inst. Chem. E* **62**, 98 (2016)
20. Ö. Gerçel, *Sep. Sci. Technol.* **51**(4), 711 (2016)
21. T. Anirudhan, M. Ramachandran, *Process Saf. Environ. Prot.* **95**, 215 (2015)
22. I. Chaari, M. Medhioub, F. Jamoussi, A.H. Hamzaoui, *J. Mol. Struct.* **12235**, 128944 (2021)
23. A. Kausar, M. Iqbal, A. Javed, K. Aftab, Z.I.H. Nazli, H.N. Bhatti, S. Nouren, *J. Mol. Liq.* **256**, 395 (2018)
24. R.P. Chiciuşă, H. Bedelea, R. Stefan, A. Măicăneanu, *J. Mol. Struct.* **1154**, 187 (2018)
25. N. Belhouchat, H. Zaghouane-Boudiaf, C. Viseras, *Appl. Clay Sci.* **135**, 9 (2017)
26. S. De Gisi, G. Lofrano, M. Grassi, M. Notarnicola, *Sustain. Mater. Technol.* **9**, 10 (2016)
27. K. Bharathi, S. Ramesh, *Appl. Water Sci.* **3**, 773 (2013)
28. M. Naushad, A.A. Alqadami, Z.A. AlOthman, I.H. Alsohaimi, M.S. Algamdi, A.M. Aldawsari, *J. Mol. Liq.* **293**, 111442 (2019)
29. T. Anithaa, P. Senthil Kumar, K. Sathish Kumar, *J. Water. Process. Eng.* **13**, 12 (2016)
30. S. Wong, N. Abd Ghafar, N. Ngadi, F.A. Razmi, I.M. Inuwa, R. Mat, N.A.S. Amin, *Sci. Rep.* **10**, 2928 (2020)
31. A. Ehsan, H.N. Bhatti, M. Iqbal, S. Noreen, *Water Sci. Technol.* **75**, 753 (2017)
32. A.M. Georgescu, F. Nardou, V. Zichil, I.D. Nistor, *Appl. Clay Sci.* **152**, 44 (2018)
33. G. Uyar, H. Kaygusuz, F.B. Erim, *React. Funct. Polym.* **106**, 1 (2016)
34. K. Li, J. Lei, G. Yuan, P. Weerachanchai, J.-Y. Wang, J. Zhao, Y. Yang, *Chem. Eng. J.* **317**, 800 (2017)
35. J. Aguiar, J. Cecilia, P. Tavares, D. Azevedo, E.R. Castellón, S. Lucena, I.S. Junior, *Appl. Clay Sci.* **135**, 35 (2017)
36. W. Hamza, C. Chtara, M. Benzina, *Res. Chem. Intermed.* **41**, 6117 (2015)
37. M. Iqbal, M. Abbas, M. Arshad, T. Hussain, A. Ullah Khan, N. Masood, M. Asif Tahir, S. Makhdoom Hussain, T. Hussain Bokhari, R. Ahmad Khera, *Pol. J. Environ. Stud.* **24**(6), 2745 (2015)
38. G. Sharma, M. Naushad, A. Kumar, S. Rana, S. Sharma, A. Bhatnagar, F.J. Stadler, A.A. Ghfar, M.R. Khan, *Process Saf. Environ. Prot.* **109**, 301 (2017)
39. J.-G. Nam, E.-S. Lee, W.-C. Jung, Y.-J. Park, B.-H. Sohn, S.-C. Park, J.S. Kim, J.-Y. Bae, *Mater. Chem. Phys.* **116**, 46 (2009)

40. H. Herbache, A. Ramdani, A. Maghni, Z. Taleb, S. Taleb, E. Morallon, R. Brahmi, Desalin. Water Treat. **57**(43), 20511 (2016)
41. A. Ramdani, Z. Taleb, A. Guendouzi, A. Kadeche, H. Herbache, A. Mostefai, S. Taleb, A. Deratani, Can. J. Chem. **98**, 79 (2020)
42. R.A. Mackay, W. Henderson, *Introduction to Modern Inorganic Chemistry*, 6th edn. (CRC Press, London, 2017)
43. L. Chmielarz, P. Kuśtrowski, Z. Piwowarska, B. Dudek, B. Gil, M. Michalik, Appl. Catal. B Environ. **88**, 331 (2009)
44. E.G. Rightor, M.-S. Tzou, T.J. Pinnavaia, J. Catal. **130**, 29 (1991)
45. T.J. Pinnavaia, M.S. Tzou, S. D. Landau, Pillared and delaminated clays containing chromium. Google Patents (1987).
46. M. Parvinzadeh, S. Eslami, Res. Chem. Intermed. **37**, 771 (2011)
47. M. Boudahri, D. Bouazza, M. Adjdir, H. Miloudi, N. Abdelkader, A. Tayeb, A. Res. Chem. Intermed. **44**, 6105 (2018)
48. M. Zahraoui, A. Mokhtar, M. Adjdir, F. Bennabi, R. Khaled, A. Djelad, A. Bengueddach, M. Sassi, Res. Chem. Intermed. **45**, 633 (2019)
49. M. Adjdir, T. Ali-Dahmane, P.G. Weidler, C. R. Chim. **12**, 793 (2009)
50. C.K. Bendeddouche, M. Adjdir, H. Benhaoua, Lett. Org. Chem. **13**, 217 (2016)
51. M. Thommes, K. Kaneko, V. Neimark Alexander, P. Olivier James, F. Rodriguez-Reinoso, J. Rouquerol, S.W. Sing Kenneth, Pure Appl. Chem. **87**, 1051 (2015)
52. F. Kooli, Microporous Mesoporous Mater. **167**, 228 (2013)
53. K.S.W. Sing, Pure Appl. Chem. **57**, 603 (1985)
54. H.-J. Muñoz, C. Vallejo, C. Blanco, A. Gil, M.-Á. Vicente, J.-H. Ramírez, L.-A. Galeano, Green Chem. **20**, 5196 (2018)
55. J.G. Carriazo, Appl. Clay Sci. **67–68**, 99 (2012)
56. P. Banković, A. Milutinović-Nikolić, Z. Mojović, N. Jović-Jovičić, M. Perović, V. Spasojević, D. Jovanović, Microporous Mesoporous Mater. **165**, 247 (2013)
57. S. Gamoudi, E. Srasra, J. Mol. Struct. **1193**, 522 (2019)
58. I. Slatni, F.Z. Elberichi, J. Duplay, N.E.H. Fardjaoui, A. Guendouzi, O. Guendouzi, B. Gasmi, F. Akbal, I. Rekkab, Environ. Sci. Pollut. Res. (2020). <https://doi.org/10.1007/s11356-020-08615-5>
59. S.K. Singh, A. Das, Phys. Chem. Chem. Phys. **17**, 9596 (2015)
60. M. Abbas, S. Kaddour, M. Trari, J. Ind. Eng. Chem. **20**, 745 (2014)
61. S. Ata, M. Imran Din, A. Rasool, I. Qasim, I. Ul Mohsin, J. Anal. Methods. Chem. **2012**(2), 405980 (2012)
62. S. Dhananasekaran, R. Palanivel, S. Pappu, J. Adv. Res. **7**, 113 (2016)
63. F. Ansari, M. Ghaedi, M. Taghdiri, A. Asfaram, Ultrason. Sonochem. **33**, 197 (2016)
64. Z. Bujňáková, M. Baláž, E. Dutková, P. Baláž, M. Kello, G. Mojžišová, J. Mojžiš, M. Vilková, J. Imrich, M. Psoška, J. Colloid Interface Sci. **486**, 97 (2017)
65. A.S. Abd-El-Aziz, A.A. Abdelghani, S.K. El-Sadany, D.P. Overy, R.G. Kerr, Eur. Polym. J. **82**, 307 (2016)
66. A.H. Jawad, N.S. Abdul Mubarak, A.S. Abdulhameed, Int. J. Biol. Macromol. **142**, 732 (2020)
67. P.F. de Sales, Z.M. Magriotis, M.A.L.S. Rossi, R.F. Resende, C.A. Nunes, J. Environ. Manag. **130**, 417 (2013)
68. P. Nidheesh, RSC Adv. **5**, 40552 (2015)

Repository KITopen

Dies ist ein Postprint/begutachtetes Manuskript.

Empfohlene Zitierung:

Kadeche, A.; Ramdani, A.; Adjdir, M.; Guendouzi, A.; Taleb, S.; Kaid, M.; Deratani, A.
Preparation, characterization and application of Fe-pillared bentonite to the removal of
Coomassie blue dye from aqueous solutions
2020. Research on chemical intermediates, 46.
doi: [10.5445/IR/1000124525](https://doi.org/10.5445/IR/1000124525)

Zitierung der Originalveröffentlichung:

Kadeche, A.; Ramdani, A.; Adjdir, M.; Guendouzi, A.; Taleb, S.; Kaid, M.; Deratani, A.
Preparation, characterization and application of Fe-pillared bentonite to the removal of
Coomassie blue dye from aqueous solutions
2020. Research on chemical intermediates, 46 (11), 4985–5008.
doi: [10.1007/s11164-020-04236-2](https://doi.org/10.1007/s11164-020-04236-2)

Lizenzinformationen: [KITopen-Lizenz](#)